Loeber, L.; Schimansky, F.P.; Kuehn, U.; Pyczak, F.; Eckert, J.:

Selective laser melting of a beta-solidifying TNM-B1 titanium aluminide alloy

In: Journal of Materials Processing Technology (2014) Elsevier

DOI: 10.1016/j.jmatprotec.2014.04.002

Selective laser melting of a beta-solidifying TNMB1 titanium aluminide alloy

Lukas Löber*[1], Frank Peter Schimansky[2], Uta Kühn[1], Florian Pyczak[2], Jürgen Eckert[1]

[1]Leibniz Institute for Solid State and Materials Research Dresden, Germany

[2]Helmholtz-Zentrum Geesthacht Centre for Materials and Coastal Research, Germany

* corresponding author: l.loeber@ifw-dresden.de Tel.: +493514659503 Fax: +493514659452

Keywords: additive manufacturing; selective laser melting; titanium aluminide; mechanical properties; optimization of process parameters

Abstract

The interest for a wider range of useable materials for the technology of selective laser melting is growing. In this work we describe a new way to optimize the process parameters for selective laser melting of a beta solidifying titanium aluminide. This kind of material has so far not been processed successfully by this method. The new approach is easy to conduct and well transferable to other materials. It is based on the fact that the parts generated from selective laser melting can be described by an addition of multiple single tracks. Multiple types of single track experiments are performed and in combination with knowledge from laser welding tests optimized parameter combinations are derived. Compact samples are built with the optimized process parameters and characterized in terms of microstructure, phase composition and mechanical properties. With this technique the generation of a TNM-B1 titanium aluminide alloy sample with a density greater than 99% could be achieved. The mechanical properties are comparable with material produced by conventional techniques.

Introduction

Selective laser melting (SLM) is an additive manufacturing technology which works layer wise and was developed from selective laser sintering. With the availability of new higher powered lasers it is now possible to fully melt the material according to Bourell et al. (1992). In SLM a laser source selectively scans a powder bed according to the CAD-data (Computer Aided Design) of the part to be produced. This three-dimensional CAD model of the desired part is always the starting point for this processing technique. It has to be divided numerically in horizontal layers of a defined thickness. In addition to the geometry, each layer contains also specific information regarding the process parameters such as laser power, scanning speed or hatching. To fix the part on the substrate material, and to enhance heat conduction during SLM processing according to Hussein et al.(2013a), support structures have to be designed. Both the CAD model and the support structure have to be sliced as described by Löber et al. (2011). These filigree support structures are built up from the same material and in the same SLM

process as the desired part and have to be removed mechanically afterwards as proposed by Hussein et al. (2013b). The complete SLM process is a number of iterations of the same procedure which consists in applying powder, melting the selected areas of the powder bed with the laser and lowering the building platform to enable the next application of a new powder layer as described by Löber et al. (2013). A schematic of the process is shown in figure 1.

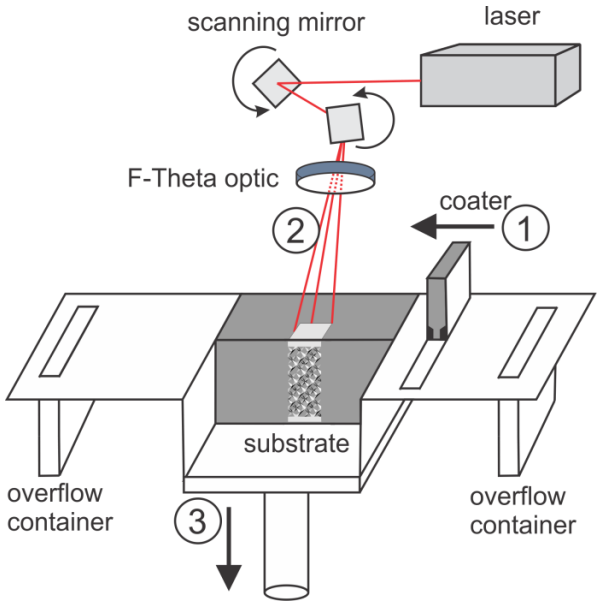

Figure 1: Schematic of SLM machine; the arrows indicate the three main process steps: 1 application of a powder layer with the coater; 2 illumination of the powder bed with the laser; 3 lowering of the platform by the layer thickness

The high intensity laser beam makes it possible to completely melt and fuse the metal powder particles together to obtain an almost fully dense material. Successive layers of metal powder particles are melted and consolidated on top of each other resulting in near-net-shaped parts as found out by Kruth (2004). Consequently, the laser melting and layered re-solidification of the powder particles is accompanied by the development of residual stresses, which arise from the high thermal gradients present in the material. This effect was discovered by Kruth et al. (2004). These stresses after Yadroitsev et al. (2013)can lead to part failure due to distortions, delamination or cracking. Besides the thermal stresses, the balling effect is also a severe impediment to interlayer connection. A last phenomenon encountered which was first described by Kruth et al.(2005)is the vaporization effect which occurs when the powder bed is irradiated with high energy intensities.

A lot of efforts are conducted to identify the crucial process parameters of SLM which influence the density of the parts as for example the work done by Mumatz et al. (2008) on Waspaloy®. The process is so far validated for a small range of different materials such as different steels, pure titanium, some titanium base alloys, Inconel, cobalt chromium and aluminium alloys. In this work we want to present the development of a suitable set of process parameters for a titanium aluminide (TiAl) alloy.

Intermetallic γ-TiAl based alloys are believed to have great potential in high temperature applications. This is mainly due to their high specific mechanical properties such as tensile strength or creep resistance at elevated temperatures according to the work of Wu et al. (2006). The low density of 3.8-4.2g/cm³ of titanium aluminides is responsible for these high specific properties. TiAl has thus become the prime candidate for replacing nickel-based super alloys in gas turbine engines. The replacement of Ni-based super alloy parts with TiAl could reduce according to the work of Voice et al. (2005) the structural weight of high performance gas turbine engines by 20-30%.Therefore, a major increase in engine performance and fuel efficiency may be realized. One of the reasons why TiAl alloys are not already widely used in engines are difficulties associated with processing.

High strength Nb bearing γ-TiAl alloys, which show only a small volume fraction of β-phase at hot-working temperature can only be forged under isothermal conditions and are extremely susceptible to cracking when tensile stresses occur which is nearly unavoidable in most forging routes. So while isothermal forging is in principle possible it is not economically feasible for most applications as demonstrated by Kremmer et al. (2008). In the past, the attractive properties of TiAl were outweighed by these difficulties in processing and machining. However, progress in manufacturing technologies as well as deeper understanding of TiAl's microstructure, deformation mechanisms, and advances in micro-alloying, have led to first commercial uses of titanium aluminides. Examples can be found in high performance turbochargers for cars and recently an US aero-engine manufacturer announced the introduction of investment cast γ-TiAl blades in the low-pressure turbine.

The so-called TNM™ alloys, as investigated in this work, are among the most promising candidates which reduce the difficulties in processing while retaining the good application properties of TiAl alloys. The name TNM is derived from niobium and molybdenum which are the main alloying elements. The overall composition of these alloys is in the range of Ti – (42–45) Al – (3–5) Nb – (0.1–2) Mo – (0.1–0.2) B (in at.%). This type of alloy is described in detail by Clemens(2008a).Niobium and molybdenum alter the phase diagram sufficiently to ensure solidification solely via the β-phase. Appel et al (2006) found out that this leads to the formation of a relatively fine grained (with d≤50 µm) microstructure in a bulk ingot after casting and the presence of a larger forging window in contrast to other high strength γ-TiAl alloys due to the presence of the disordered bcc β-phase at forging temperature.The β-phase provides a sufficient number of independent slip systems and therefore acts as a deformation accommodating phase during forging according to Schloffer et al. (2012). Nevertheless, the alloy composition is balanced in such a way that serious compromises in high temperature capability at application temperature are avoided.

Experimental

The starting material with a nominal composition of Ti-Al28.9-Nb9.68-Mo2.26-B0.024 wt.% was bought as an alloyed rod from the company GfE Gesellschaft für Elektrometallurgie mbH. The material was gas-atomized by the EIGA method (Electrode Induction-melting Gas Atomization). The process is well described by Gerling et al.(2004). The process works crucible-free under a protective argon atmosphere. In this technique the pre-alloyed rod dips into a conical induction coil. Upon operation of the coil the tip of the rod is heated and melts. This melt pours through the center of a gas nozzle and is atomized by

argon gas (purity 99.999%). The powder was collected and sieved into four different batches: 0-45 µm, 45-63 µm, 63-95 µm and 95-125 µm. In this work, only the batch of 45-63 µm was used. The resulting powder can be seen in figure 2.The chemical composition of rod, powder and SLM material was measured via ICP-OES (inductively coupled plasma optical emission spectrometry).

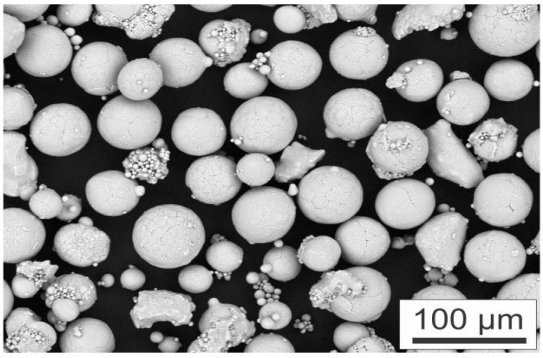

Figure 2: Morphology of the TNM-B1 powder (batch 45-63 µm)

Additionally, for comparison three rods with a diameter of 3 mm and a length of 40 mm were cast in a centrifugal casting machine high term titan 3.3 from the company Linn from the starting rod material. A conventional process route was seen apt for this comparison. 20 g of the starting rod material was placed in the casting machine. The machine was evacuated to a pressure of 10^{-5} mbar and then flooded with argon gas (purity 99.999%). The material was heated via an induction coil till melting occurred. The temperature of the melt during casting was around 1773 K.

The SLM experiments were performed on a commercially available SLM 250 hl machine (SLM Solutions GmbH). The machine is equipped with a 400 W Nd-YAG fiber laser which works in continuous mode, has a wavelength of 1075 nm and a spot size of approximately 80 µm in the focus. Before the illumination of the powder bed starts the building chamber is flooded with argon (purity 99.999%) until the residual oxygen content is below 200 ppm. The building chamber works under an overpressure of around 10 mbar. During the process the build chamber is monitored by two oxygen detectors. Residual oxygen levels of less than 200 ppm can thus be guaranteed.

For the single track experiments a layer of approximately 50 µm in thickness was applied on a titanium-base substrate. It has to be mentioned that the layer thickness might vary in a certain range (±10 µm) depending on the substrate roughness, particularities of powder delivering, leveling and spreading, and granulomorphometric characteristics of the powder.

Three different single track experiments with different parameter combinations were performed under the otherwise same experimental conditions. Only laser power and scanning speed were changed during the experiments. The used parameter combinations were the following:

Table 1: Overview of the parameter combinations including the line energy input

Scanning speed / Laser power	350 mm/s	700 mm/s	1050 mm/s	1400 mm/s	1750 mm/s	2100 mm/s
50 W	2.88 J/mm²	2.4 J/mm²	1.92 J/mm²	1.44 J/mm²	0.96 J/mm²	0.48 J/mm²
100 W	5.76 J/mm²	4.8 J/mm²	3.84 J/mm²	2.88 J/mm²	1.92 J/mm²	0.96 J/mm²
150 W	8.64 J/mm²	7.2 J/mm²	5.76 J/mm²	4.32 J/mm²	2.88 J/mm²	1.44 J/mm²
200 W	11.52 J/mm²	9.6 J/mm²	7.68 J/mm²	5.76 J/mm²	3.84 J/mm²	1.92 J/mm²
250 W	14.29 J/mm²	12.0 J/mm²	9.6 J/mm²	7.2 J/mm²	4.8 J/mm²	2.4 J/mm²

Cont Table 1: Overview of the parameter combinations including the line energy input

Scanning speed / Laser power	50 mm/s	60 mm/s	70 mm/s	80 mm/s	90 mm/s	100 mm/s
50 W	20.00 J/mm²	16.67 J/mm²	14.29 J/mm²	12.50 J/mm²	11.11 J/mm²	10.00 J/mm²
100 W	40.00 J/mm²	33.33 J/mm²	28.57 J/mm²	25.00 J/mm²	22.22 J/mm²	20.00 J/mm²
150 W	60.00 J/mm²	50.00 J/mm²	42.86 J/mm²	37.50 J/mm²	33.33 J/mm²	30.00 J/mm²
200 W	80.00 J/mm²	66.67 J/mm²	57.14 J/mm²	50.00 J/mm²	44.44 J/mm²	40.00 J/mm²
250 W	100.00 J/mm²	83.33 J/mm²	71.43 J/mm²	62.50 J/mm²	55.56 J/mm²	50.00 J/mm²

Cont Table 1: Overview of the parameter combinations including the line energy input

Scanning speed / Laser power	100 mm/s	150 mm/s	200 mm/s	250 mm/s	300 mm/s	350mm/s
50 W	10.00 J/mm²	6.67 J/mm²	5.00 J/mm²	4.00 J/mm²	3.33 J/mm²	2.86 J/mm²
100 W	20.00 J/mm²	13.33 J/mm²	10.00 J/mm²	8.00 J/mm²	6.67 J/mm²	5.71 J/mm²
150 W	30.00 J/mm²	20.00 J/mm²	15.00 J/mm²	12.00 J/mm²	10.00 J/mm²	8.57 J/mm²
200 W	40.00 J/mm²	26.67 J/mm²	20.00 J/mm²	16.00 J/mm²	13.33 J/mm²	11.43 J/mm²
250 W	50.00 J/mm²	33.33 J/mm²	25.00 J/mm²	20.00 J/mm²	16.67 J/mm²	14.29 J/mm²

For each parameter set two single tracks were produced in different substrate positions for comparison.

Based on the results from the single track experiments overlapping experiments with different hatchings were performed. The preparation and execution of the experiment was similar to the single track experiments.

The last set of SLM experiments included the production of cylinders for mechanical testing and microstructural analysis as well as some dodecahedron unit cells as representative of a more complex 3D structure. The process parameters used for these specimens were: laser power 100 W, scanning speed 50 mm/s for the volume contour, laser power 175 W and scanning speed 1000 mm/s for the outer contour, a hatching of 0.3 mm, and a layer thickness of 75 µm. The used scanning strategy was a stripe hatching. A detailed description of the different process parameters is given by (Louvis et al., 2011).

Heat treatment of selected cast and SLM samples was performed as a two-step heat treatment as shown in figure 3.

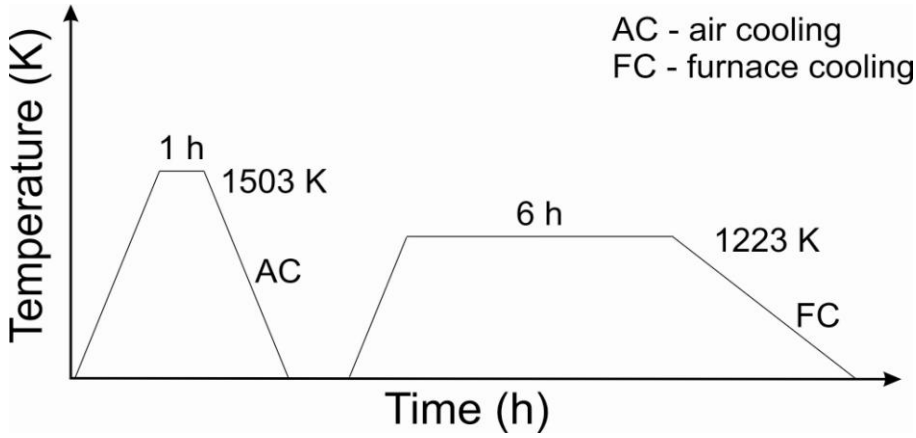

Figure 3: Schematic of the applied heat treatment

The heat treatment was conducted in air which leads to oxidation in the surface region. The heat treatment conditions were chosen from the work of Clemens et al. (2008b). In his work he describes the microstructural evolution caused by different heat treatments.

The surface of the single tracks was characterized with an optical microscope (Keyence VHX 2000) and a scanning electron microscope (LEO 1530 Gemini from the company Zeiss). The width of the melt tracks was measured with the VHX analyzing software. Selected specimens from the single track experiments were cut with a Struers Accutom 5. The samples were embedded into epoxy resin and metallographically prepared with a Rotopol. The specimens were grinded with decreasing grit size from 300 to 4000 and then polished with colloidal SiO particle with a size of 50 nm. The samples were then

etched for 10 seconds with Kroll's agent (92 ml distilled water, 6 ml nitric acid and 2 ml hydrofluoric acid). The same preparation except the last etching step was performed for the compact specimens which were characterized with a LEO 1530 Gemini scanning electron microscope from the company Zeiss in backscattered electron mode. One of the compression samples was cut into pieces for X-ray diffraction (XRD). X-ray analysis was also conducted on the powder material. Structural characterization was performed by X-ray diffraction using a D3290 PANalytical X'pert PRO with Co-Kα radiation (λ = 0.17889 nm) in Bragg-Brentano configuration.

The density of the specimens was measured via the Archimedes method with a Sartorius density measuring set YDK-01 (0D).

Mechanical testing of the compression samples was performed on an Instron 5869 testing device. The compression samples were cut coplanar with a rotating cup wheel. The cast samples had a diameter of 3 mm and a height of 6 mm while the samples from SLM had a diameter of 4 mm and a height of 8 mm. The strain rate was set constant to 0.01 mm/sec. The strain was measured via a laser extensometer (Fiedler Optoelektronik GmbH) and 4 attached reference measuring stripes on the samples. For each condition, at least three samples were tested. The mechanical testing was performed at room temperature.

Results and Discussion

Powder

The morphology of the atomized powder is spherical. The chemical composition was only changed to a minor extent due to the atomization process (see table 1). The aluminium content is slightly lower while the molybdenum content is slightly elevated. This is probably caused by the low boiling point of aluminium which caused evaporation during the atomization process. The flowability of the powder was tested with a modified hall flow meter. To better simulate the conditions of the SLM machine, the diameter of the hall flow meter was changed from 2.45 mm as demanded in DIN EN ISO 4490to 3 mm. With this setup a full cylinder was emptied after 15.82 sec.

Table 2: Chemical composition of the TNM rod material, powder material and SLM sample

Element (wt.%)	Titanium	Aluminum	Niobium	Molybdenum	Boron
rod material	balance	28.90	9.68	2.26	0.024
powder	balance	28.49	9.38	2.32	0.030
SLM	balance	28.45	9.40	2.30	0.028

Single track morphology

The variation of the scanning speed and the laser power has a great influence on the morphology of the melt tracks. Six different types of melt tracks could be identified (see figure 3). At low laser power (50 W) and slow scanning speeds (50-100 mm/s), but also at intermediate laser power (100 W) and very high scanning speeds (350-2100 mm/s), balling could be observed. The same effect was observed by Toloochko et al. (2004).According to his work is the effect of surface tension responsible for the molten pool to assume the general shape of a circular or segmental cylinder. Furthermore fragmentation of the tracks called balling effect is a well-known drawback of SLM. This is interesting because the balling effect described by Louvis et al. (2011) is observed for the combination of high powers and slow scanning speeds. The balling at higher scanning speeds can be explained by the Plateau–Rayleigh capillary instability of the melt pool which was described by Gusarov (2007). Two factors normally stabilize the process with decreasing scanning speeds: reduction of the length-to-width ratio of the melt pool and increase of the width of its contact with the substrate. The instability of a liquid cylinder was initially described by Rayleigh(1878) and further by Nichols and Mullins (1965). Their analyses show that a cylinder of water is unstable in front of sinusoidal fluctuations when the wavelength λ is greater than the cylinder circumference $2\pi R$. The reduction of the surface energy with decreasing surface area is the driving force for the break-up of the liquid cylinder. However, there are various other parameters which influence the balling effect. An incomplete list according to Yadroitsev et al. (2007) include laser powder, layer thickness, substrate material, physical properties and granulomorphometry of the powder. A recording of such a balling can be seen in figure 4 a).

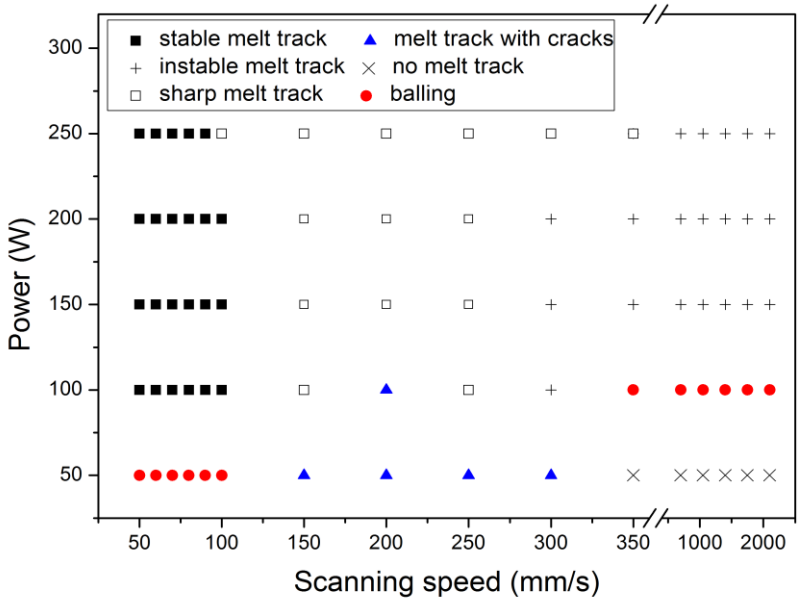

Figure 4: Process map of the single track experiments with the indication of the different observed melt track morphologies

Combining a low laser power of 50 W with high scanning speeds >350 mm/s does not lead to the formation of a visible melt track. It can be assumed that the line energy input of less than 2 J/mm² was either not sufficient to melt the powder and fuse it to the substrate or the powder was melted by the

laser but the used energy input was too low to create a joint molten pool. In this case the powder would form rounded free surfaces as published in the work of Yadroitsev et al. (2010).

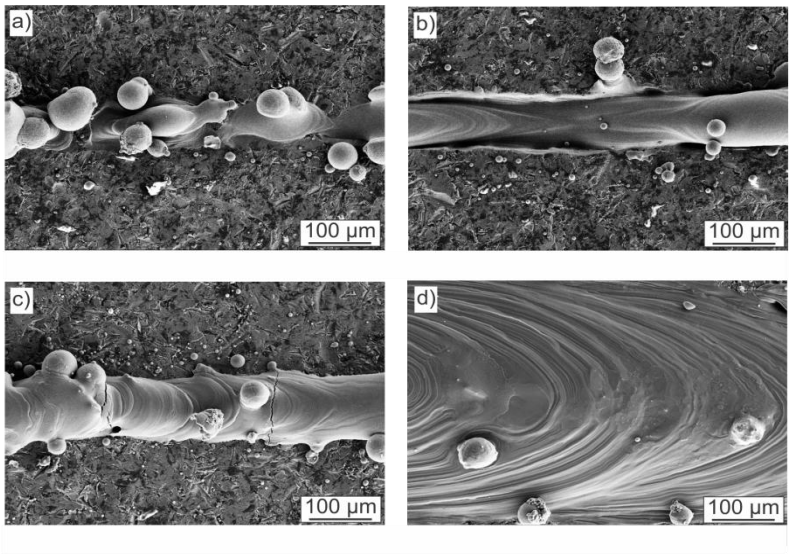

Figure 5: Different melt track morphologies: (a) balling, (b) instable melt track, (c) melt track with cracks and (d) stable melt track

Staying at higher scanning speeds and increasing the power changes the morphology from balling to an instable melt track, as already mentioned above. The discussed morphology can be seen in figure 4 b). Such instable melt tracks were already described by Niuand Chang (1999) with steel powder. They identified the oxygen content of the powder as main reason for the instabilities. In this case, the instabilities are probably caused by a bad connection between the melt track and the adjacent substrate. Also Childset al. (2004) showed instable melt tracks in their work on different steel powders. Unfortunately, no explanation was given for this phenomenon. A possible explanation might be found in the work of Kruth (2004). In this work the phenomenon of evaporation during the exposure of the powder particles is discussed. The vapor can interact with the laser radiation, becomes ionized and forms a plasma which decreases the laser power in the powder.

When going to lower scanning speeds (150-300 mm/s) at low power, melt tracks with pronounced cracks perpendicular to the scanning direction could be observed. A typical example is displayed in figure 4 c). The shape of the track is similar to the ones where balling occurs but with the addition of multiple cracks. In literature, the problem of crack formation in the melt zone is often described for welding of titanium aluminides as for example discussed in the work of Guoqing et al. (2011). The crack formation is most probably associated with the high cooling rate during solidification, leading to residual stresses which are relieved by the formation of cracks.

Quite a broad range of parameter combinations in the intermediate region (scanning speed: 150-300 mm/s; laser power: 100-250 W) leads to stable melt tracks without balling or crack formation. The shape of these single tracks is quite sharp. In the field of welding such well-defined weld tracks are often associated with segregations and crack formation along the weld track. This effect is circumstantiated by

Anik and Dorn (1995). The material at the solidification front has a lower solidification temperature due to micro segregations compared to the already solidified material. Therefore, the resistance against shrinkage is reduced and solidification cracks might form more easily. All the so far described parameter combinations were not further investigated due to their inherent problems.

The last morphology which could be found is a stable and smooth melt track for slow scanning speeds (50-100 mm/s) and intermediate to high laser powers (100-250 W) (for visualization, see figure 4d)). In this case, the combination of a small super cooling of the liquid and a high thermal gradient leads to stalk-like solidification which is generally associated with low segregations. The surface of the melt track is even and the width of the track stays constant. These parameter sets seem appropriate for the process of selective laser melting and for the production of fully dense parts. In addition to the top surface observations, metallographic investigations of the cross sections for the single tracks with a speed of 50 mm/s were conducted. The resulting micrographs can be seen in figure5. The change in laser powers has a quite significant influence on the morphology of the melt tracks. When using a low power of 50 W most of the energy is concentrated in the powder material (see figures5 a) and c)). The molten pool forms free circular cylinder with the ratio $\pi D/L \leq 1$; therefore a capillary instability appears. Only a small amount of the substrate is molten for this set of parameters which might lead to a bad interface between the melt and the substrate. It has to be taken into consideration that this micrograph only reflects a snap-shot. Since this parameter combination is prone to the balling effect, the cross section will look different a couple of µm away. With increasing power (150 W) the change is quite drastic (see figures5 b) and e)). The width of the track is more than tripled and the interaction with the substrate becomes more intense. The classic zones of a melt track can be properly observed: from the melting zone inside, over the zone of partial melting (darker area around the melting zone) and the heat-affected zone (bright area around the zone of partial melting) to the unaffected substrate. This indicates a good interaction between the melt pool and the substrate and guarantees a good fusion between both. When further increasing the power to 250 W the width of the melt track becomes even broader (see figures 5 c) and f)). Again all the classic zones of a melt track are well observable. The depth of the track is further increased to around 600 µm which would correspond to more than 10 layers of material. In addition a huge pore in the lower part of the finger-shaped melt track can be observed. This wormhole is generally caused when intermediate cooling rates are present. The solidification rate is higher than the buoyancy velocity of the entrapped gas in the melt. Another explanation might be due to an abnormal material flow during welding. Boldsaikhan et al. (2011) gave this explanation in their work for similar results. Since this is an undesired defect in the melt track, the parameter set with the lower power, where the defect is not that pronounced, was chosen for the further experiments. The width of each single track was recorded at 10 different points and an average was made from the measurements. The width varies from 110± 5.8 µm for a power of 50 W and a speed of 100 mm/s to a width of 704 ± 18.5 µm for a power of 250 W and a speed of 50 mm/s, respectively. The dependence between the width of the melt track and the used laser power is roughly linear.

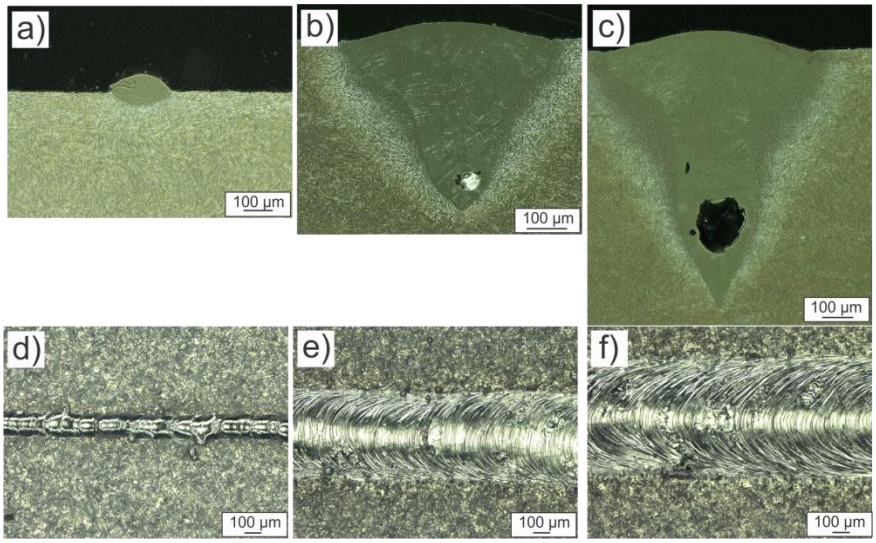

Figure 6: Top and cross section view (after etching with Kroll) of melt tracks with different process parameters (a) and (d) P: 50 W, v: 50 mm/s; (b) and (e) P: 150 W, v: 50 mm/s, (c) and (f) P: 250 W, v: 50 mm/s

To investigate the interaction between multiple scan tracks and to determine an optimal hatching, different experiments with overlapping scan tracks were conducted with a power of 150 W and a scanning speed of 50 mm/s. Similar to the single track experiments a thin layer of powder was applied and multiple scan tracks were placed with different distances next to each other. The measured width of the single track was taken, and accordingly overlaps of 25% and 50%, which correspond to a hatching of 0.2 mm and 0.3 mm, were conducted. The top views of these experiments can be seen infigure 6. Both experiments show a good and stable overlapping of the melt tracks. Since no apparent difference in the quality could be observed, a hatching of 0.3 mm corresponding to an overlap of 50% was chosen for the production of compact samples. By this, the amount of tracks which are needed, and thus the building time of the parts, is reduced.

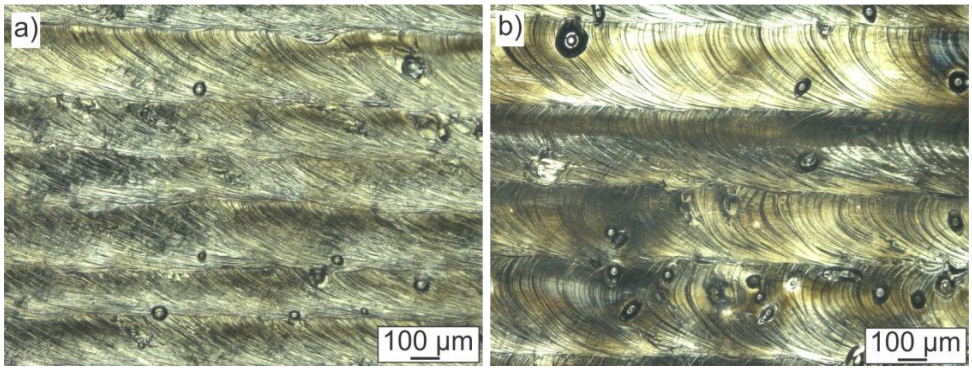

Figure 7: Top view of the hatching experiments, P: 150 W, v: 50 mm/s, a) dx: 0.2 mm and b) dx: 0.3 mm

Compact samples

Three of the produced compact cylindrical samples were removed from the substrate plate, freed of the support structure, cut co-parallel and their density was measured via the Archimedes method. First the density of the starting material was measured and taken as 100% relative density. A density of 4.144 g/cm³ could be measured for the starting rod material. The SLM cylinders displayed a density of 4.102-4.122 g/cm³ which corresponds to a relative density of 98.89-99.46%.The residual porosity could be determined from a micrograph as small spherical pores (diameter 20-50 µm) evenly distributed throughout the material. This could either be caused by wormholes built during the solidification or by entrapped gas in the powder material as described by Biamino et al. (2010). The chemical composition of the samples was not affected by the SLM process (see table 1).

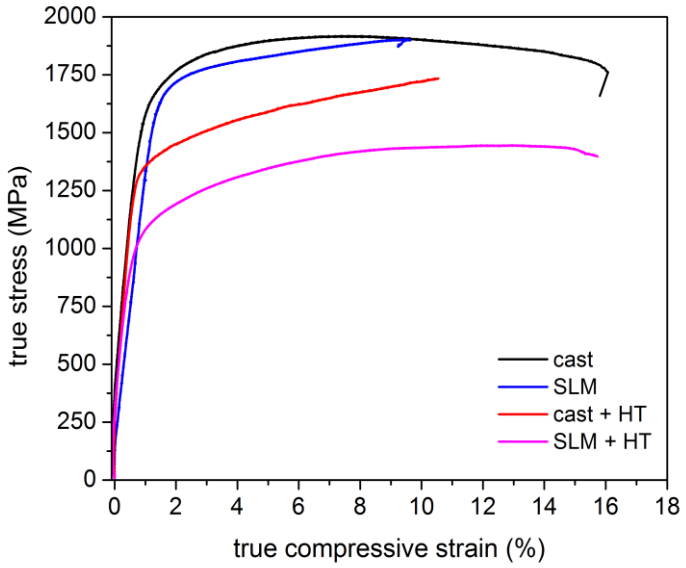

Figure 8: True stress strain diagrams from the compression testing

Table 3: Characteristic values from the compression test for the cast and SLM samples

	Offset Yield Strength (MPa)	Ultimate Strength (MPa)	Ultimate Strain (%)
Cast	1611-1685	1918-2012	8.14-10.59
SLM	1620-1651	1816-1903	4.5-9.5
Cast + HT	1302-1324	1728-1768	12.3-15.4
SLM + HT	886-1071	1428-1671	12.3-16.5

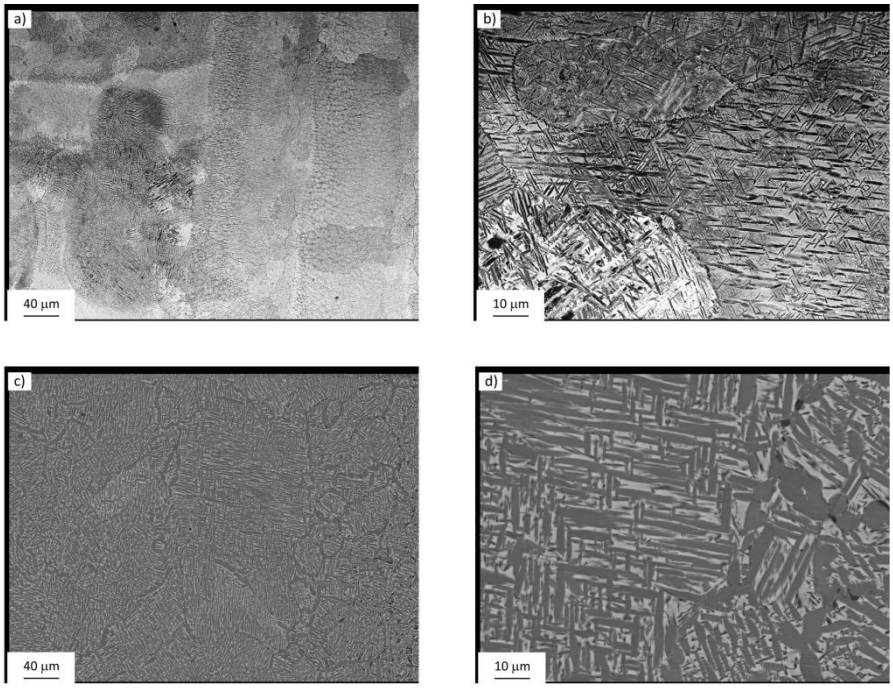

Figure 9: SEM pictures of the a), b) SLM produced TNM sample and c), d) the corresponding heat treated sample (view is perpendicular to the building direction)

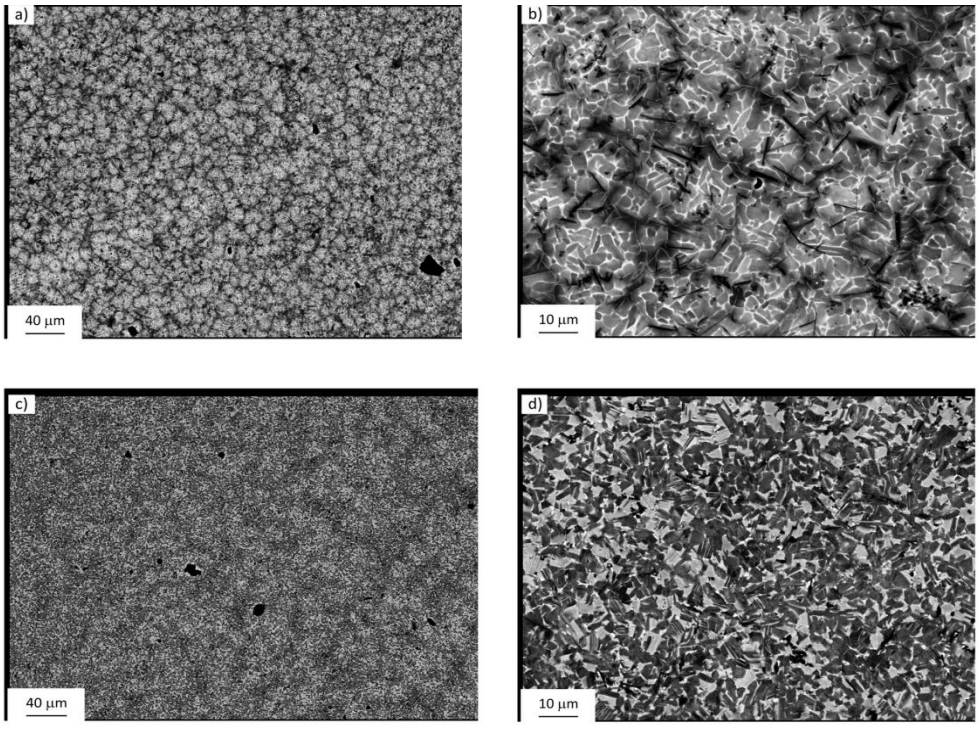

Figure 10: SEM pictures of the a), b) cast sample and c), d) the corresponding heat treated sample

Samples from the SLM process were prepared for compression testing, metallographic preparation and phase analysis. The corresponding microstructures can be seen in figure 8. The microstructure of the produced cast and heat treated samples are shown in figure 9.Selected results from the compression tests of the SLM, cast, SLM heat-treated and cast heat-treated sample are shown in figure 7. The results from all the specimens are summarized in table 2.The mechanical performance of the SLM samples is slightly lower compared to the conventional cast sample. A possible explanation for this fact can either be found in the residual porosity of the SLM samples compared to the fully compact cast samples or in the microstructure of the specimens. It is noteworthy, that the cast samples also showed some porosity which can be seen in figure 9. The microstructure in z-direction of the build job of the SLM sample before and after heat-treatment is shown in figure 8. The microstructure of the SLM sample can be described as nearly lamellar β. The darker areas in the micrograph show the α_2 phase, while the brighter bone-like features correspond to the β-phase. The nearly lamellar β microstructure is associated with high strength, high creep strength and moderate room temperature ductility according to the work of Schweighofer et al.(2011). The two phases could also be identified by X-ray diffraction (see figure 10). The microstructural features clearly indicate that solidification occurred via the β-phase, i.e. L → L + β → β → …, followed by a multitude of solid-state transformations and reactions. It is supposed that the reaction $\alpha_2 \rightarrow (\alpha_2 + \gamma)_L$ did not take place. The microstructure is not homogenous in the SLM sample and regions with coarser and finer microstructure are found next to each other as visible in figures 8 a) and b). This probably stems from local differences in the cooling rate during the SLM process. The heat treated sample reveals a slightly different microstructure (compare figure 8 b) and d)). Again the brighter areas correspond to the β-phase with darker α_2 phase regions in between. But in some positions of the broader β lamellae dark finer lamellae can be observed. Here the partial transformation from β to γ phase occurred. In general the microstructure coarsened during the heat treatment compared with the SLM sample. The three phases β, α_2 and γ can also be identified via X-ray diffraction. The applied two step heat treatment caused a microstructural homogenization in the first step at 1503 K in the α/β-region and allowed the precipitation of γ lamellae in the second step at 1223 K. While it is not clearly discernible from the SEM micrographs the cast heat treated sample seems to display a lower content of β-phase compared to the SLM heat treated sample, visible from the lower intensity of the corresponding XRD peaks around 48° and 68° (see figure 10). The microstructures of the cast and the cast and heat treated samples are shown in figure 9. In the as cast microstructure (figure 9 a) and b)) fine segregations of heavier elements probably niobium and molybdenum appear as bright regions in the backscattered electron image. In higher magnification it is discernible that the microstructure is composed from a bright phase with a branch like structure embedded in regions of a darker phase. In conjunction with the XRD data the brighter phase is identified as remnant β regions embedded in α_2-phase. Black lines in figure 9 b) stem from borides which fell off during the specimen preparation. Subsequent to heat treatment a duplex structure consisting of β and α_2 grains with some γ lamellae in α_2/γ colonies is found. In general the cast microstructures tend to be finer and more isotropic than the corresponding SLM microstructures. This difference is especially pronounced when comparing the SLM and heat treated with the cast and heat treated sample. This finer microstructure is probably the main reason why the cast samples exhibit in average a higher strength than the respective SLM specimen state.

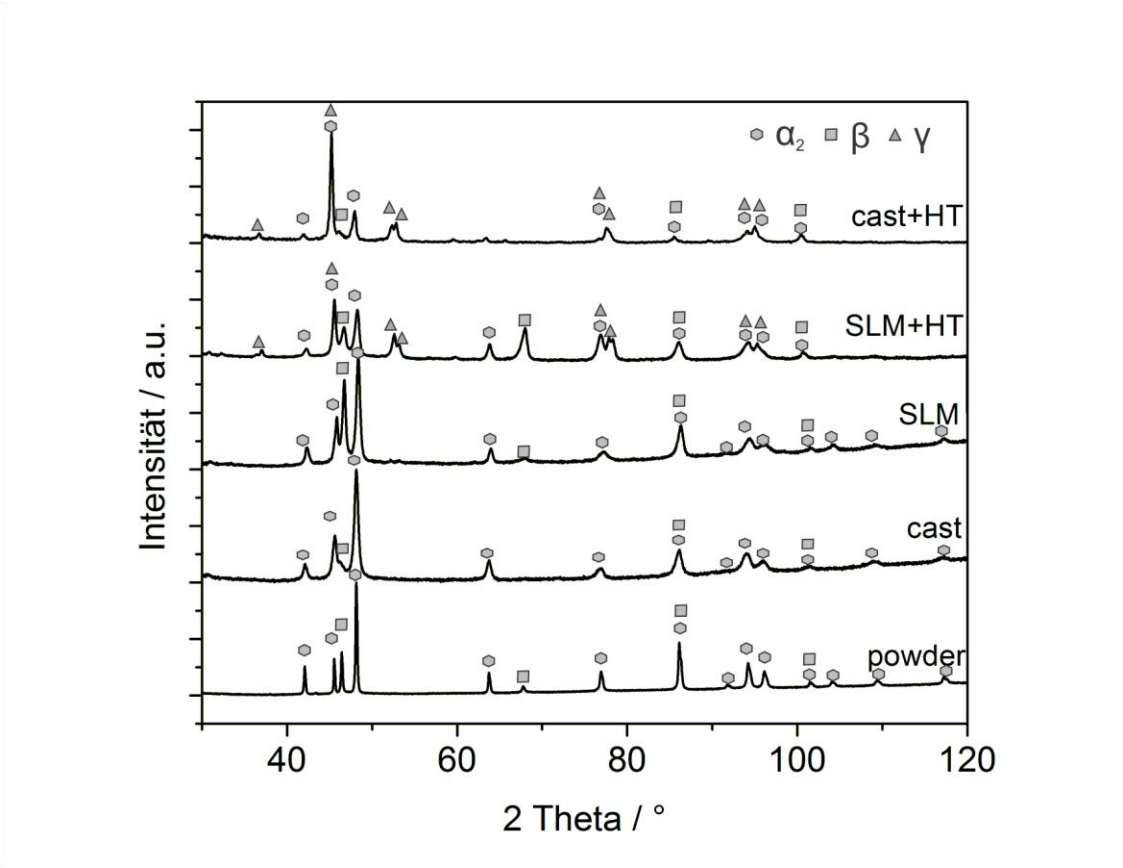

Figure 11: X-Ray diffraction patterns of the TNM powder, the cast sample, the SLM sample and the heat treated SLM sample

Figure 12: Produced TNMB1 3D-dodecahedron structures with optimized parameter set

Conclusions

In this work an easy and fast method of optimizing the process parameters for a new difficult to process alloy for selective laser melting was demonstrated. Starting from single tracks with various parameter combinations six different melt track morphologies could be identified: insufficient melting, balling, melt tracks with cracks, instable melt tracks, sharp melt tracks and round stable melt tracks. For high laser power settings, wormholes were found in the cross section of otherwise stable melt tracks. From experiments with overlapping melt tracks, an optimal hatching for the best combination of laser power and scanning speed was identified. The optimized parameter set consist of the following parameter values: laser power 100 W, scanning speed 50 mm/s for the volume contour, laser power 175 W and scanning speed 1000 mm/s for the outer contour, a hatching of 0.3 mm, and a layer thickness of 75 µm. The scanning strategy was a stripe hatching. These optimized parameters were applied for the production of bulk cylinders and dodecahedron unit cells as shown in figure 12. A relative density of around 99% and a fine grained nearly lamellar β microstructure was achieved. The mechanical performance of the samples is comparable to conventional cast samples. Heat treatment of the samples leads to the formation of γ phase.

Acknowledgements

This research was funded by the European Union and the Free State of Saxony (13795/2379) in the framework of the European Centre for Emerging Materials and Processes (ECEMP).The authors are grateful to S. Donath for the execution of the casting experiments as well as S. Neumann for the conduction of the heat treatments.

Figure 1: Schematic of SLM machine; the arrows indicate the three main process steps: 1 application of a powder layer with the coater; 2 illumination of the powder bed with the laser; 3 lowering of the platform by the layer thickness

Figure 2: Morphology of the TNM-B1 powder (batch 45-63 µm)

Figure 3: Schematic of the applied heat treatment

Figure 4: Process map of the single track experiments with the indication of the different observed melt track morphologies

Figure 5: Different melt track morphologies: (a) balling, (b) instable melt track, (c) melt track with cracks and (d) stable melt track

Figure 6: Cross and top section views (after etching with Kroll' agent) of melt tracks with different process parameters (a) and (d) P: 50 W, v: 50 mm/s; (b) and (e) P: 150 W, v: 50 mm/s, (c) and (f) P: 250 W, v: 50 mm/s

Figure 7: Top view of the hatching experiments, P: 150 W, v: 50 mm/s, (a) dx: 0.2 mm and (b) dx: 0.3 mm

Figure 8: True stress-true strain diagrams from the compression testing

Figure 9: SEM pictures of the (a), (b) SLM produced TNM sample and (c), (d) the corresponding heat treated sample (view is perpendicular to the building direction)

Figure 10: SEM pictures of the (a), (b) cast sample and (c), (d) the corresponding heat treated sample

Figure 11: X-Ray diffraction patterns of the TNM powder, the cast sample, the SLM sample and the heat treated SLM sample

Figure 12: Produced TNMB1 3D-dodecahedron structures with optimized parameter set

References

Anik, S., Dorn, L., 1995. Schweißeignung metallischer Werkstoffe. DVS Verlag.

Appel, F., Oehring, M., Paul, J.D.H., 2006. Nano-Scale Design of TiAl Alloys Based on beta-Phase Decomposition. Advanced Engineering Materials 8 371-376

Biamino, S., Penna, A., Ackelid, U., Sabbadini, S., Tassa, O., Fino, P., Pavese, M., Gennaro, P., Badini, C., 2010. Electron beam melting of Ti-48Al-2Cr-2Nb alloy: Microstructure and mechanical properties investigation. Intermetallics.

Boldsaikhan, E., Corwin, E.M., Logar, A.M., Arbegast, W.J., 2011. The use of neural network and discrete Fourier transform for real-time evaluation of friction stir welding. Applied Soft Computing 11 4839 - 4846

Bourell, D.L., Marcus, H.L., Barlow, J.W., Beaman, J.J., 1992. Selective laser sintering of metals and ceramics. Int. J. Powder Metall 28 369

Childs, T.H.C., Hauser, C., Badrossamay, M., 2004. Mapping and Modelling Single Scan Track Formation in Direct Metal Selective Laser Melting. CIRP Annals - Manufacturing Technology 53 191 - 194

Clemens, H., Chladil, H.F., Wallgram, W., Zickler, G.A., Gerling, R., Liss, K.D., Kremmer, S., Güther, V., Smarsly, W., 2008a. In and ex situ investigations of the beta-phase in a Nb and Mo containing beta-TiAl based alloy. Intermetallics 16 827 - 833

Clemens, H., Wallgram, W., Kremmer, S., Güther, V., Otto, A., Bartels, A., 2008b. Design of Novel β-Solidifying TiAl Alloys with Adjustable β/B2-Phase Fraction and Excellent Hot-Workability. Advanced Engineering Materials 10, 707-713.

Gerling, R., Clemens, H., Schimansky, F.P., 2004. Powder Metallurgical Processing of Intermetallic Gamma Titanium Aluminides. Advanced Engineering Materials 6, 23-38.

Guoqing, C., Binggang, Z., Wei, L., Jicai, F., 2011. Crack formation and control upon the electron beam welding of TiAl-based alloys. Intermetallics 19 1857 - 1863

Gusarov, A.V., Yadroitsev, I., Bertrand, P., Smurov, I., 2007. Heat transfer modelling and stability analysis of selective laser melting. Applied Surface Science 254, 975-979.

Hussein, A., Hao, L., Yan, C., Everson, R., 2013a. Finite element simulation of the temperature and stress fields in single layers built without-support in selective laser melting. Materials & Design 52, 638-647.

Hussein, A., Hao, L., Yan, C., Everson, R., Young, P., 2013b. Advanced lattice support structures for metal additive manufacturing. Journal of Materials Processing Technology 213, 1019-1026.

Kremmer, S., Chladil, H., Clemens, H., Otto, A., Güther, V., 2008. Near conventional forging of titanium aluminides. The Japan Institute of Metals (JIM) 6, 989-992

Kruth, J.P., Froyen, L., Vaerenbergh, J.V., Mercelis, P., Rombouts, M., Lauwers, B., 2004. Selective laser melting of iron-based powder. Journal of Materials Processing Technology 149 616 - 622
Kruth, J.P., Mercelis, P., Van Vaerenbergh, J., Froyen, L., Rombouts, M., 2005. Binding mechanisms in selective laser sintering and selective laser melting. rapid prototyping journal 11, 26-36.
Löber, L., Flache, C., Petters, R., Kühn, U., J., E., 2013. Comparison of different post processing technologies for SLM generated 316l steel parts. rapid prototyping journal 19, 173-179.
Löber, L., Klemm, D., Kühn, U., Eckert, J., 2011. Rapid Manufacturing of Cellular Structures of Steel or Titaniumalumide. Materials Science Forum 690, 130.
Louvis, E., Fox, P., Sutcliffe, C.J., 2011. Selective laser melting of aluminium components. Journal of Materials Processing Technology 211, 275-284.
Mumtaz, K.A., Erasenthiran, P., Hopkinson, N., 2008. High density selective laser melting of Waspaloy®. Journal of Materials Processing Technology 195 77 - 87
Nichols, F.A., Mullins, W.W., 1965. Surface-(Interface-) and volume-diffusion contributions to morphological changes driven by capillarity. Trans. Metall. Soc. AIME 233 1840-1848
Niu, H.J., Chang, I.T.H., 1999. Instability of scan tracks of selective laser sintering of high speed steel powder. Scripta Materialia 41 1229 - 1234
Rayleigh, L., 1878. On The Instability Of Jets. Proc. London Math. Soc. 10 4
Schloffer, M., Iqbal, F., Gabrisch, H., Schwaighofer, E., Schimansky, F.-P., Mayer, S., Stark, A., Lippmann, T., Göken, M., Pyczak, F., Clemens, H., 2012. Microstructure development and hardness of a powder metallurgical multi phase γ-TiAl based alloy. Intermetallics 22, 231-240.
Schweighofer, E., Schloffer, M., Schmoelzer, T., Mayer, S., Lindemann, J., Guether, V., Klose, J., H., C., 2011. Microstructural optimization of a cast and hot-isostatically pressed TNM alloy by heat treatments, 4th international TiAl Workshop, Nueremberg.
Tolochko, N.K., Mozzharov, S.E., Yadroitsev, I.A., Laoui, T., Froyen, L., Titov, V.I., Ignatiev, M.B., 2004. Balling processes during selective laser treatment of powders. rapid prototyping journal 10, 78-87.
Voice, W.E., Henderson, M., Shelton, E.F.J., Wu, X., 2005. Gamma titanium aluminide, TNB}. Intermetallics 13 959 - 964
Wu, X.H., 2006. Review of alloy and process development of TiAl alloys. Intermetallics 14, 1114-1122.
Yadroitsev, I., Bertrand, P., Smurov, I., 2007. Parametric analysis of the selective laser melting process. Applied Surface Science 253 8064 - 8069
Yadroitsev, I., Gusarov, A., Yadroitsava, I., Smurov, I., 2010. Single track formation in selective laser melting of metal powders. Journal of Materials Processing Technology 210 1624 - 1631
Yadroitsev, I., Krakhmalev, P., Yadroitsava, I., Johansson, S., Smurov, I., 2013. Energy input effect on morphology and microstructure of selective laser melting single track from metallic powder. Journal of Materials Processing Technology 213, 606-613.

Figure 1

Click here to download high resolution image

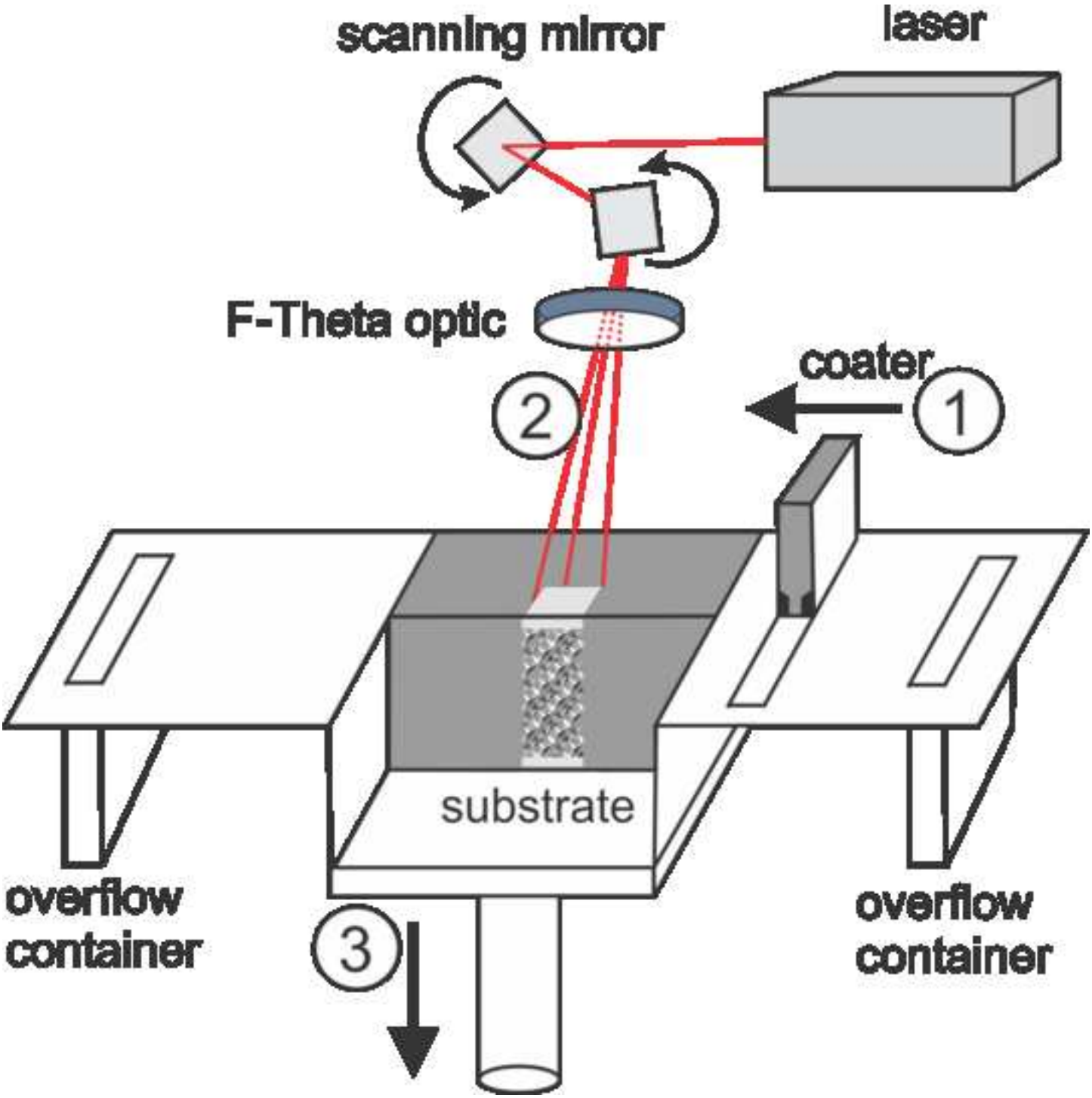

Figure 2

Click here to download high resolution image

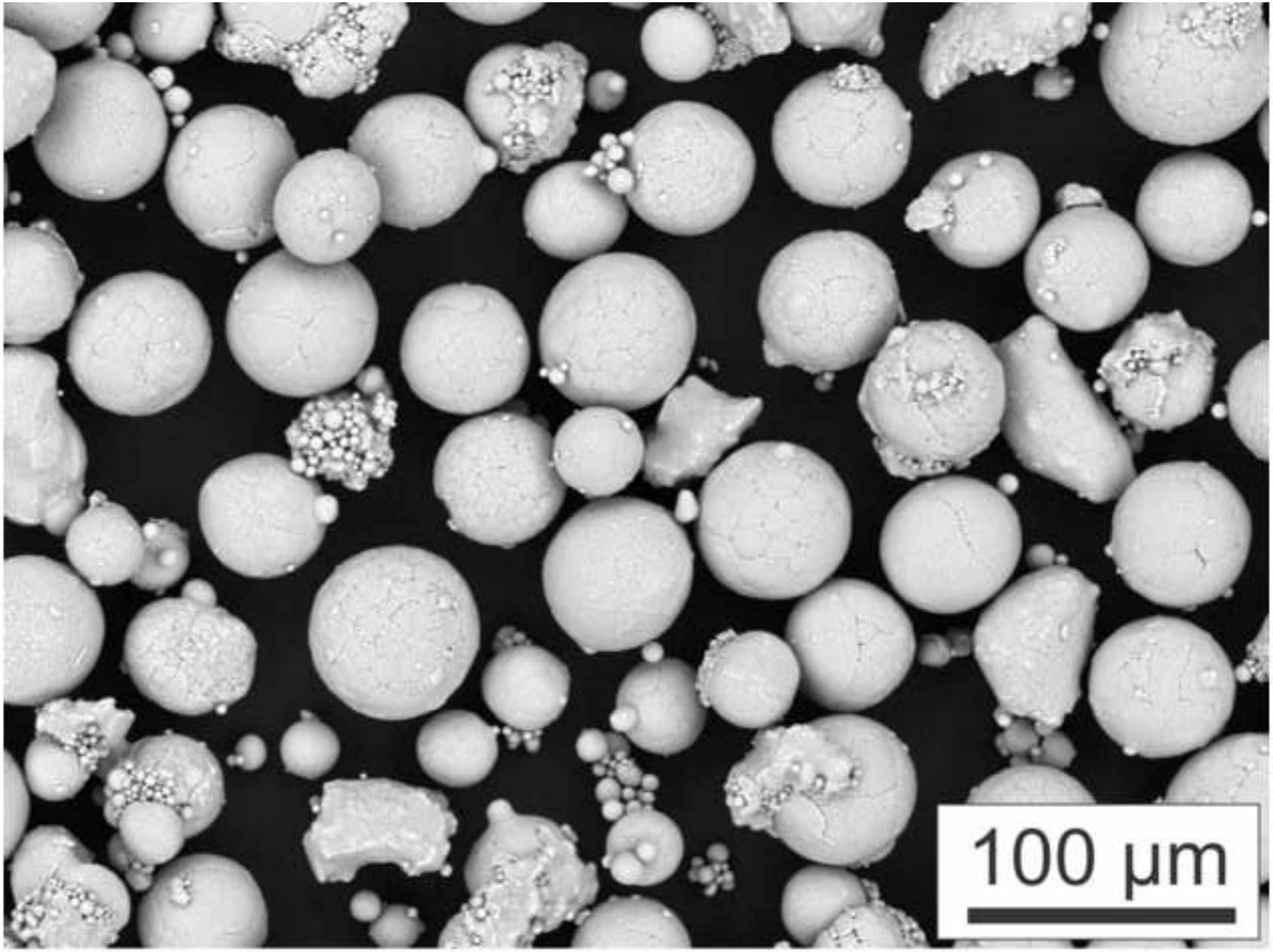

Figure 3
Click here to download high resolution image

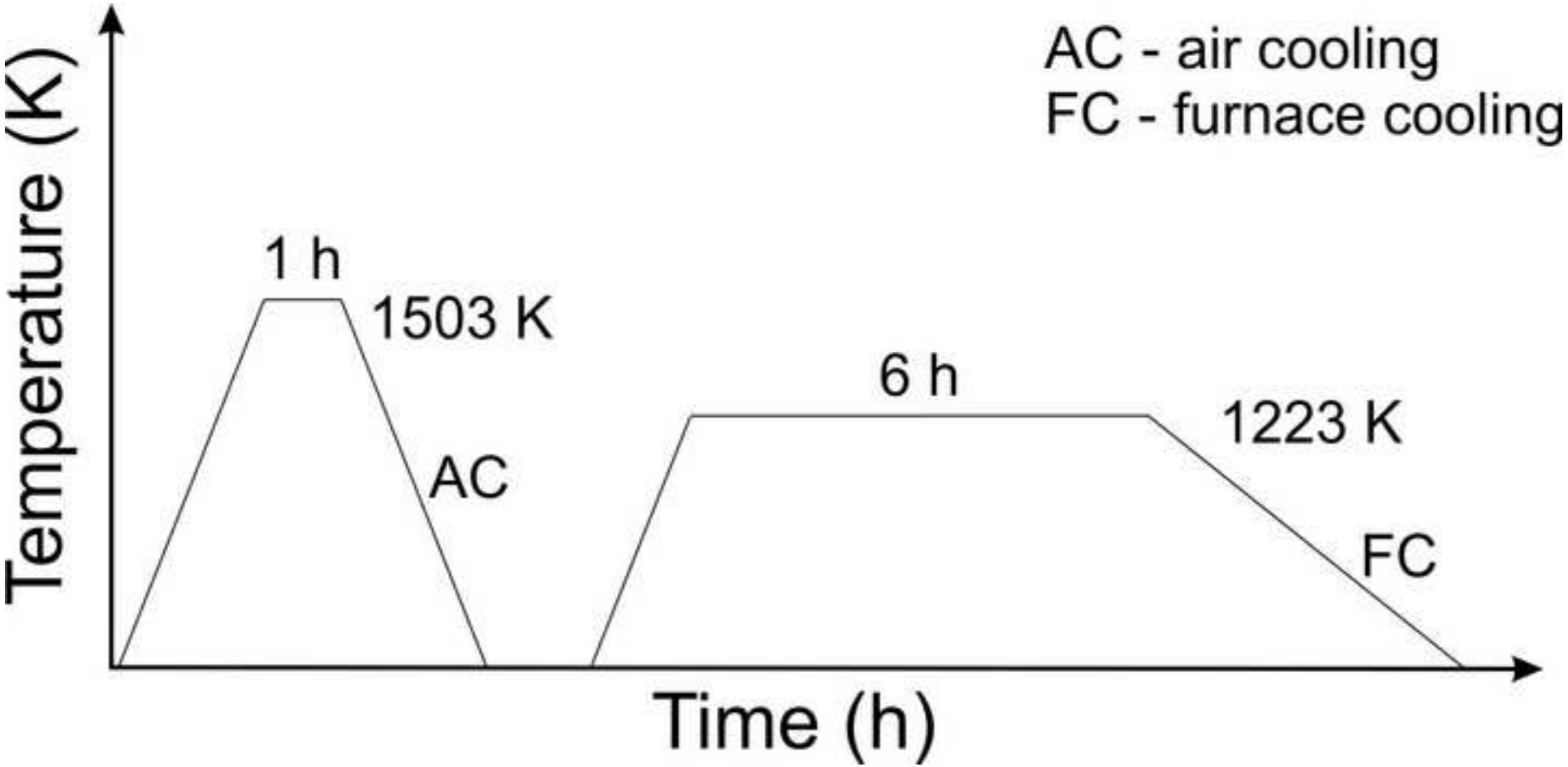

Figure 4

Click here to download high resolution image

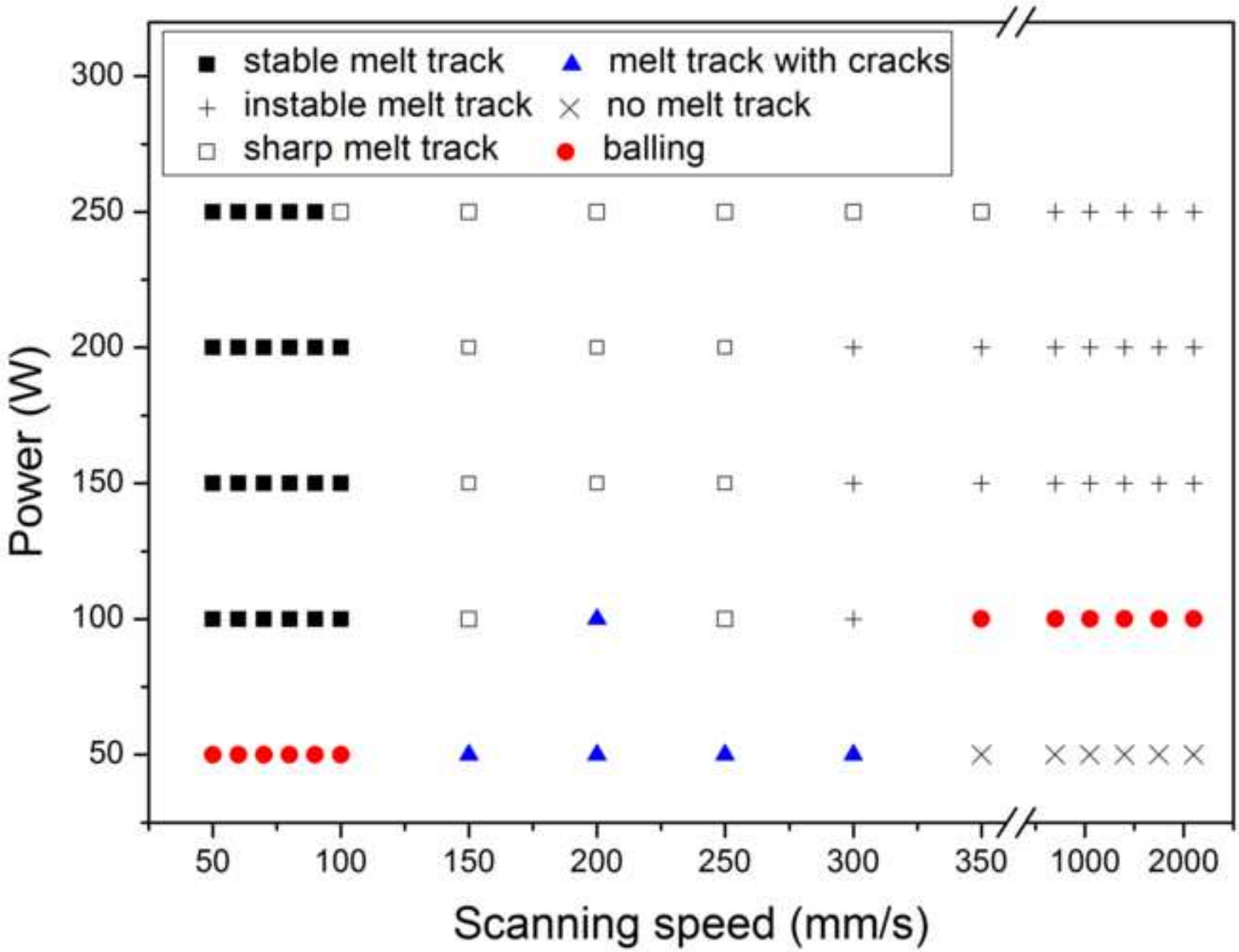

Figure 5

Click here to download high resolution image

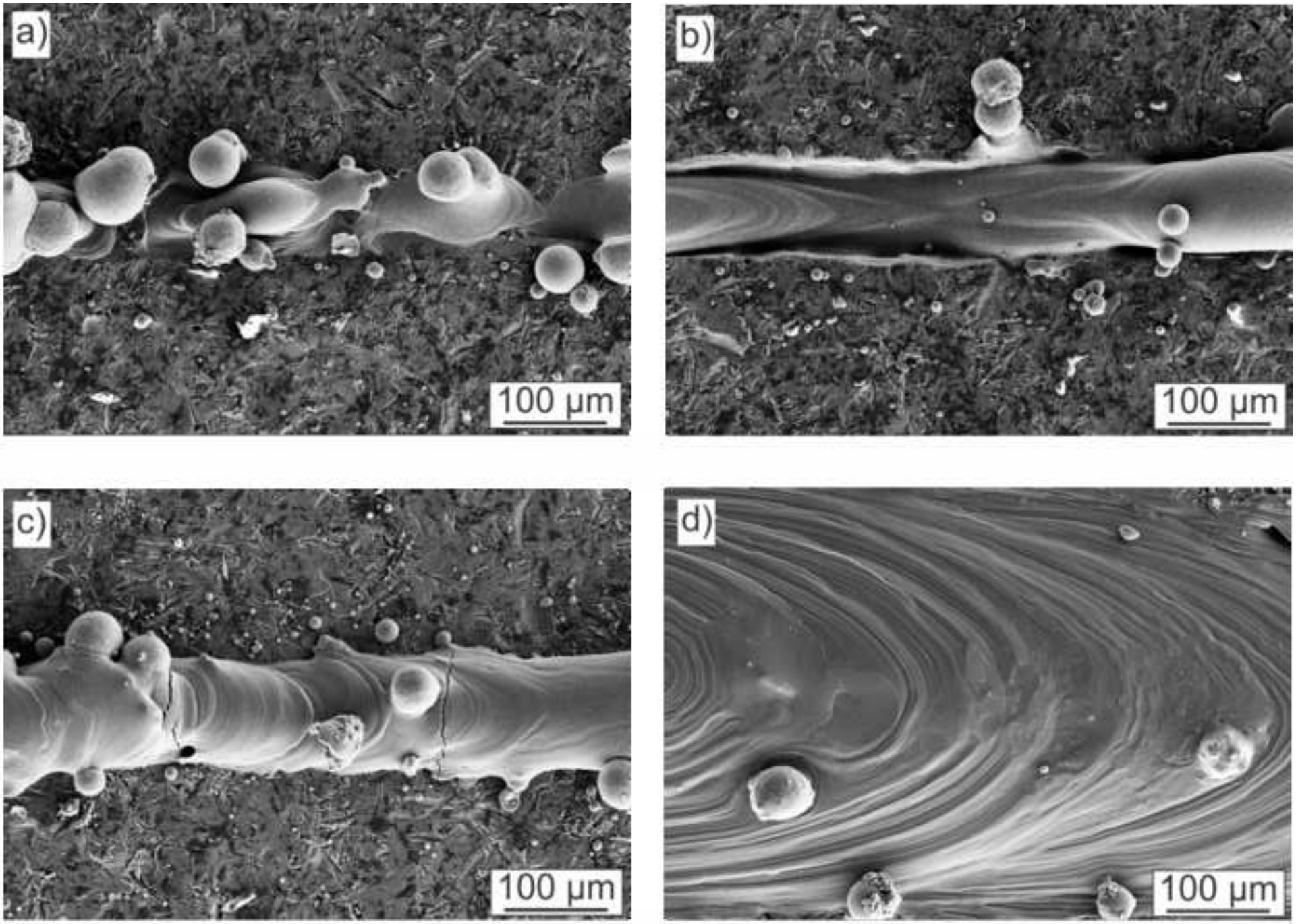

Figure 6

Click here to download high resolution image

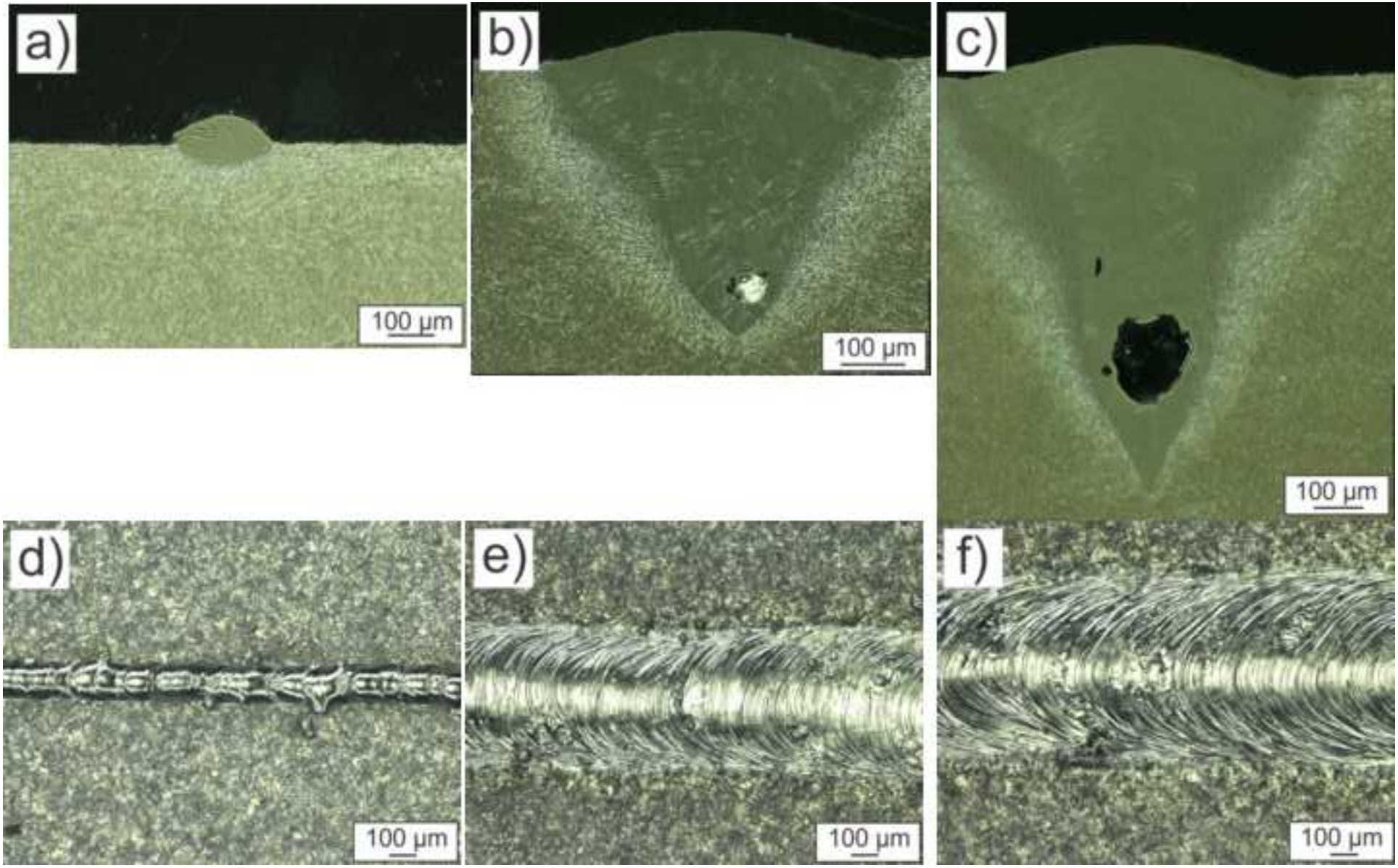

Figure 7

Click here to download high resolution image

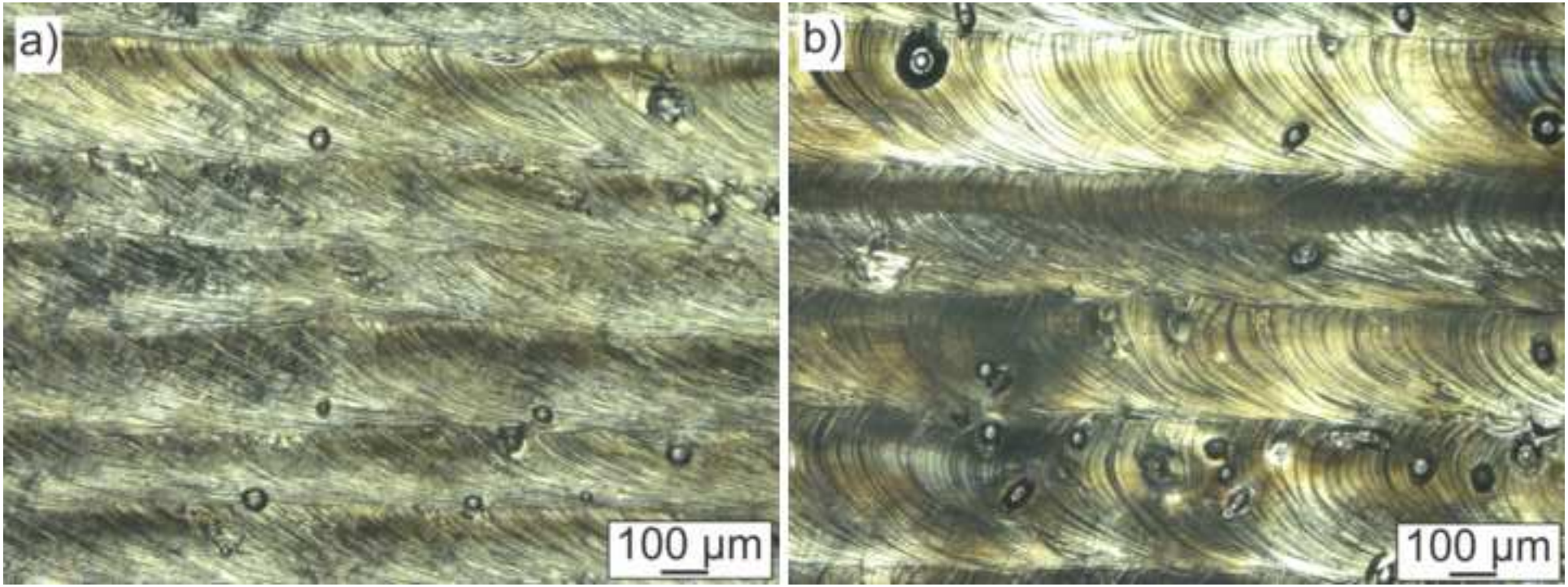

Figure8

Click here to download high resolution image

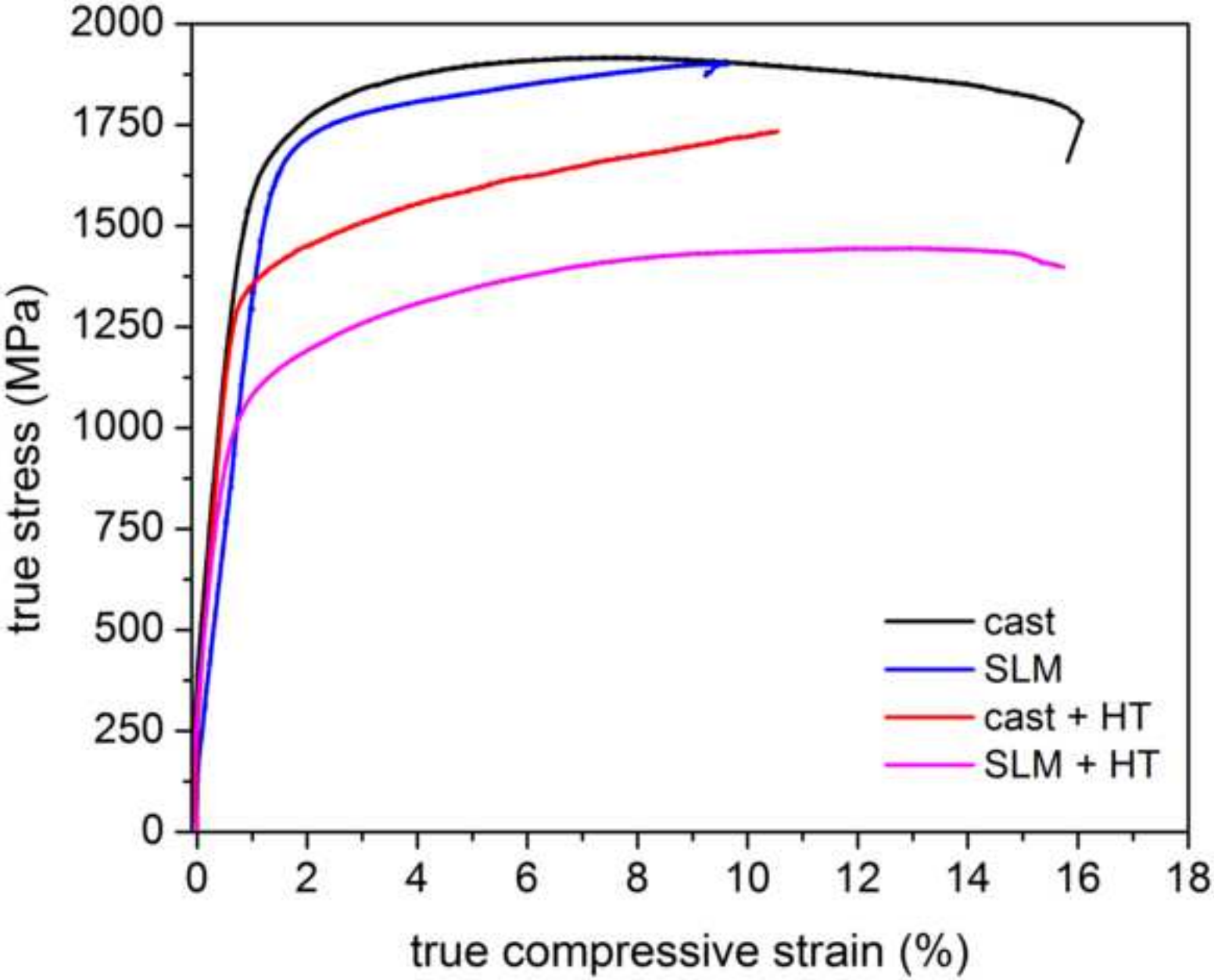

Figure 9

Click here to download high resolution image

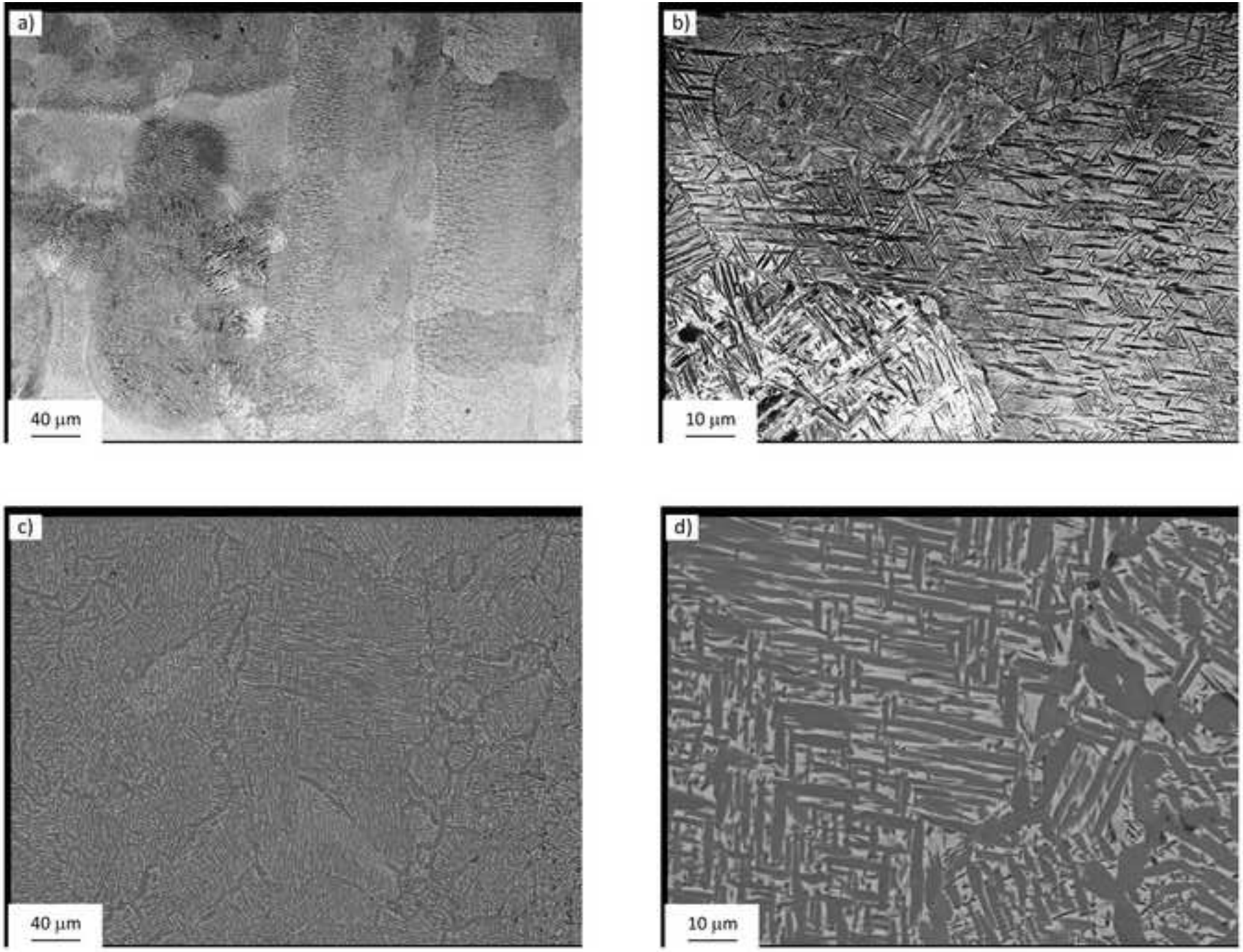

Figure 10

Click here to download high resolution image

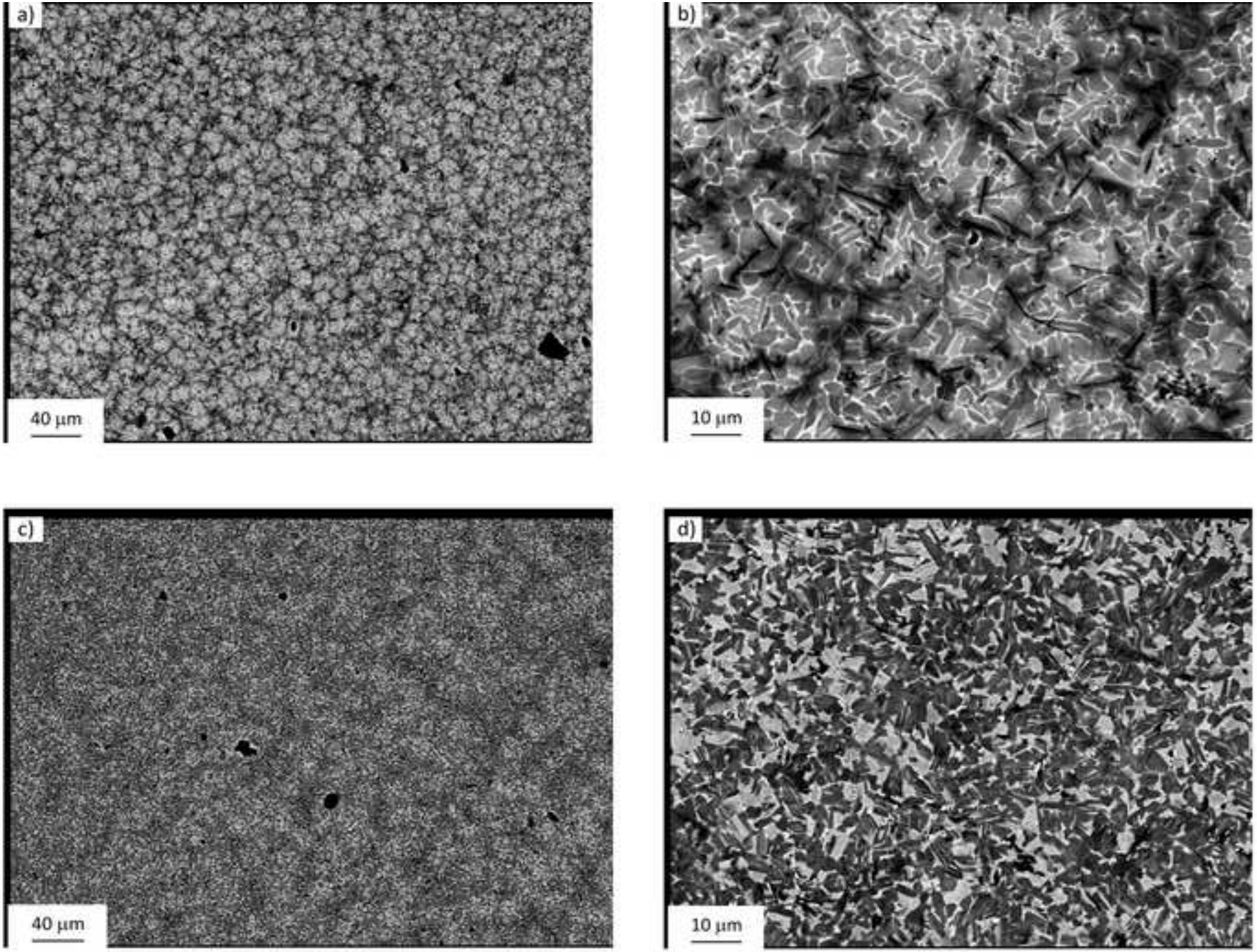

Figure 11

Click here to download high resolution image

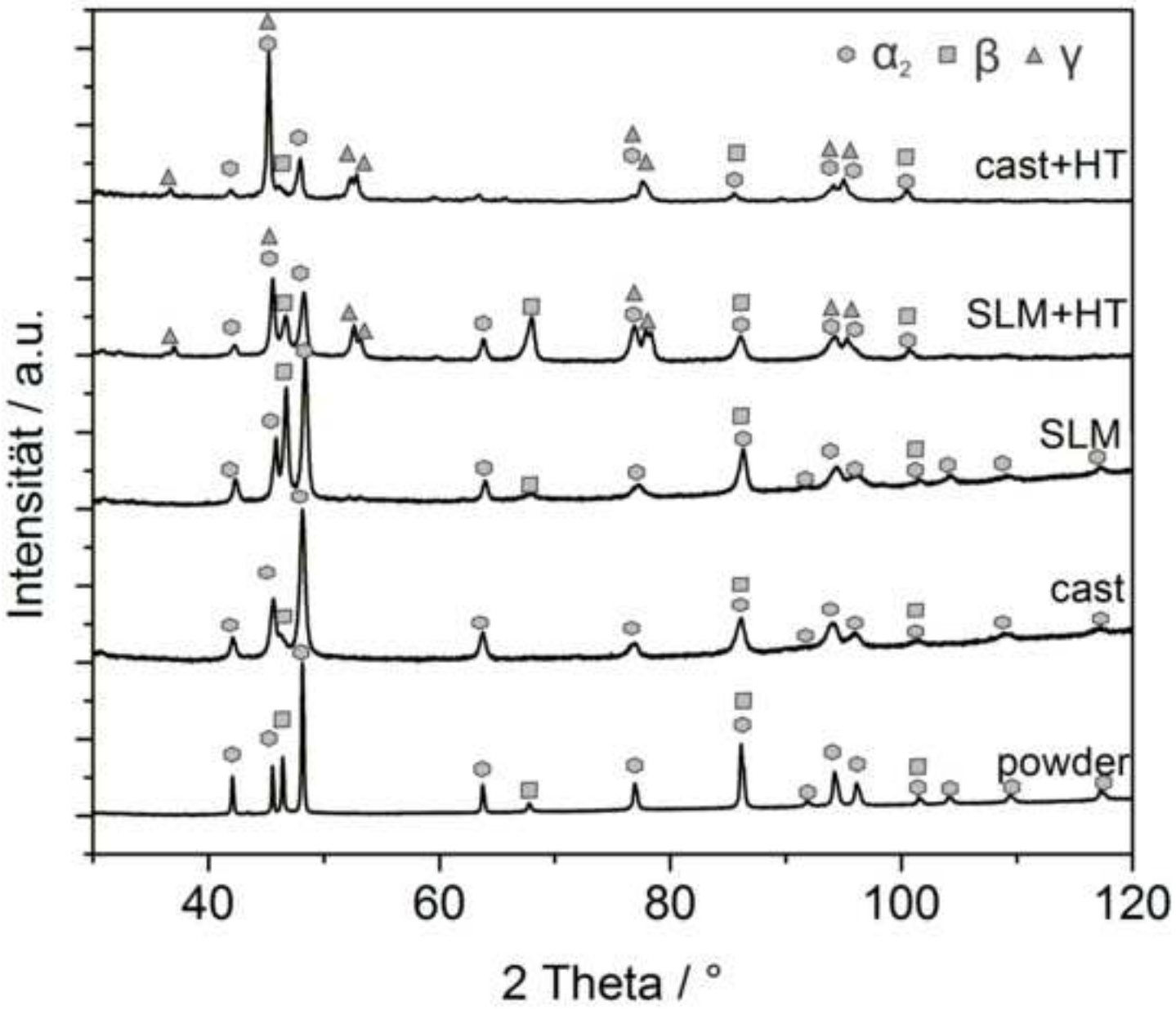

Figure 12

Click here to download high resolution image

Tables

Table 1: Overview of the parameter combinations including the line energy input

Comment [l1]: Changed text about process parameters into a table as suggested by reviewer 1 + 2

Scanning speed / Laser power	350 mm/s	700 mm/s	1050 mm/s	1400 mm/s	1750 mm/s	2100 mm/s
50 W	2.88 J/mm²	2.4 J/mm²	1.92 J/mm²	1.44 J/mm²	0.96 J/mm²	0.48 J/mm²
100 W	5.76 J/mm²	4.8 J/mm²	3.84 J/mm²	2.88 J/mm²	1.92 J/mm²	0.96 J/mm²
150 W	8.64 J/mm²	7.2 J/mm²	5.76 J/mm²	4.32 J/mm²	2.88 J/mm²	1.44 J/mm²
200 W	11.52 J/mm²	9.6 J/mm²	7.68 J/mm²	5.76 J/mm²	3.84 J/mm²	1.92 J/mm²
250 W	14.29 J/mm²	12.0 J/mm²	9.6 J/mm²	7.2 J/mm²	4.8 J/mm²	2.4 J/mm²

Cont Table 1: Overview of the parameter combinations including the line energy input

Scanning speed / Laser power	50 mm/s	60 mm/s	70 mm/s	80 mm/s	90 mm/s	100 mm/s
50 W	20.00 J/mm²	16.67 J/mm²	14.29 J/mm²	12.50 J/mm²	11.11 J/mm²	10.00 J/mm²
100 W	40.00 J/mm²	33.33 J/mm²	28.57 J/mm²	25.00 J/mm²	22.22 J/mm²	20.00 J/mm²
150 W	60.00 J/mm²	50.00 J/mm²	42.86 J/mm²	37.50 J/mm²	33.33 J/mm²	30.00 J/mm²
200 W	80.00 J/mm²	66.67 J/mm²	57.14 J/mm²	50.00 J/mm²	44.44 J/mm²	40.00 J/mm²
250 W	100.00 J/mm²	83.33 J/mm²	71.43 J/mm²	62.50 J/mm²	55.56 J/mm²	50.00 J/mm²

Cont Table 1: Overview of the parameter combinations including the line energy input

Scanning speed / Laser power	100 mm/s	150 mm/s	200 mm/s	250 mm/s	300 mm/s	350mm/s
50 W	10.00 J/mm²	6.67 J/mm²	5.00 J/mm²	4.00 J/mm²	3.33 J/mm²	2.86 J/mm²
100 W	20.00 J/mm²	13.33 J/mm²	10.00 J/mm²	8.00 J/mm²	6.67 J/mm²	5.71 J/mm²

150 W	30.00 J/mm²	20.00 J/mm²	15.00 J/mm²	12.00 J/mm²	10.00 J/mm²	8.57 J/mm²
200 W	40.00 J/mm²	26.67 J/mm²	20.00 J/mm²	16.00 J/mm²	13.33 J/mm²	11.43 J/mm²
250 W	50.00 J/mm²	33.33 J/mm²	25.00 J/mm²	20.00 J/mm²	16.67 J/mm²	14.29 J/mm²

Table 2: Chemical composition of the TNM rod material, powder material and SLM sample

Element (wt.%)	Titanium	Aluminum	Niobium	Molybdenum	Boron
rod material	balance	28.90	9.68	2.26	0.024
powder	balance	28.49	9.38	2.32	0.030
SLM	balance	28.45	9.40	2.30	0.028

Table 3: Characteristic values from the compression test for the cast and SLM samples

	Offset Yield Strength (MPa)	Ultimate Strength (MPa)	Ultimate Strain (%)
Cast	1611-1685	1918-2012	8.14-10.59
SLM	1620-1651	1816-1903	4.5-9.5
Cast + HT	1302-1324	1728-1768	12.3-15.4
SLM + HT	886-1071	1428-1671	12.3-16.5